International Journal for Numerical and Analytical Methods in Geomechanics

WILEY

RESEARCH ARTICLE OPEN ACCESS

Investigation of Suffusion Under Torsional Shear Conditions With CFD-DEM

Shun-Xiang Song[1] | Zhen-Yu Yin[1] | Ya-Jing Liu[2] | Pei Wang[3] | Yi-Pik Cheng[4]

[1]Department of Civil and Environmental Engineering, The Hong Kong Polytechnic University, Kowloon, China | [2]College of Civil Engineering, Zhejiang University of Technology, Hangzhou, China | [3]Jiangxi Key Laboratory of Infrastructure Safety Control in Geotechnical Engineering, East China Jiaotong University, Nanchang, China | [4]Department of Civil, Environmental and Geomatic Engineering, University College London, London, UK

Correspondence: Zhen-Yu Yin (zhenyu.yin@polyu.edu.hk)

Received: 16 June 2024 | **Revised:** 13 August 2024 | **Accepted:** 10 September 2024

Funding: This study is supported by the Research Grants Council of Hong Kong (Project No. 15209119, 15226322, 15229223) and the National Natural Science Foundation of China (Project No. 42207210).

Keywords: coupled CFD-DEM method | HCTST | intermediate principal stress ratio | pore structure | principal stress rotation | suffusion

ABSTRACT

This study investigates, for the first time ever, the suffusion on gap-graded granular soils under torsional shear conditions from a microscopic perspective. A numerical model of the hollow cylinder torsional shear test (HCTST) using the discrete element method (DEM) is first developed, where an algorithm for simulating the real inner and outer rubber membranes of the hollow cylinder apparatus (HCA) is introduced. After the validation, the computational fluid dynamics (CFD) approach is introduced for the coupling between the particle and fluid phases. Then, a series of the coupled CFD-DEM suffusion simulations considering the rotation of the major principal stress axis (α) and intermediate principal stress ratio (b) are conducted. It is found that more fine particles are eroded in cases having smaller α and b, and the clogging phenomenon in the middle zones becomes more significant as both α and b increase. From the microscopic perspective, the specimens whose contact anisotropy principal direction is close to the fluid direction will lose more fines, and the anisotropy magnitude also plays an important role. In addition, the differences in structure and vertical connectivity of the pores in HCTST samples under various complex loading conditions cause fine particles to have different migration paths, further resulting in different fines mass loss.

1 | Introduction

As a typical kind of internal erosion, suffusion is regarded as one of the most common causes of the failure of hydraulic structures [1]. During the suffusion process, the fine particles are observed to detach from the coarse particles and migrate through the pores inside the soil structure subjected to the impact of seepage flow [2, 3]. This complex fluid–particle interaction has been proven to be linked to many factors, including the particle size distribution (PSD), particle shape, fines content (FC) and hydraulic gradient [4–12]. Recently, considering the complex in situ stress conditions in different zones of the hydraulic structures, some physical experiments have been conducted to investigate the effect of stress states on suffusion [5, 13–16]. For example, Chang and Zhang [14] conducted a series of laboratory tests using a stress-controlled apparatus and found that the increase of the deviatoric stress would result in the increase of the maximum erosion rate and deformation of the soil specimen. Then, some hydro-mechanical coupling tests on gap-graded soils under isotropic, triaxial compression and triaxial extension stress paths were designed. A higher initiation hydraulic gradient was observed in the suffusion test under the extension stress condition [5]. Luo et al. [16] further found that there is a piece-wise linear relationship between the critical initiation hydraulic gradient and deviator stress by a series of physical suffusion tests.

Compared with the physical experiments, the coupled computational fluid dynamics-discrete element method (CFD-DEM) method can provide an insight into the microscopic mechanism of suffusion [17–21]. Xiong et al. [22] presented a coupled CFD-DEM method to investigate the suffusion in a coarse-grained skeleton and analysed the evolution of force network and the effect of pore size on clogging. Qian et al. [11] studied the evolution of contact anisotropy parameters and the flow paths of fine particles in the gap-graded soils during erosion. Within the coupled CFD-DEM method, the fluid phase, particle system and fluid-particle interaction can be studied separately. The rearrangements of particles and force chains, the different pressure gradients in different zones of the specimen and the drag force on each particle can be accurately captured during the suffusion [22–25]. Therefore, researchers can have a better understanding of the effect of stress states on suffusion. For example, Hu et al. [26] investigated the micro-mechanisms of initial stress anisotropy on the suffusion and subsequent shear behaviours of gap-graded soils by monitoring and analysing the evolution of coordination number and fabric anisotropy. The confining pressure and FC were observed having a coupled effect on suffusion: the increase in the confining pressure would intensify the suffusion when FC was large, while a negligible effect was observed when FC was small [27]. Zhou et al. [28] investigated the internal erosion of gap-graded sandy soil under isotropic, triaxial compression and triaxial extension conditions using the coupled CFD-DEM approach and found that the anisotropy magnitude of the isotropic specimen remained constant, while that in the other two specimens showed a decreasing trend during the erosion process. In their work, the microscopic behaviours including the coordination numbers of both coarse and fine particles, typical erosion paths of fine particles and force chain networks were analysed in detail, and the superiority of the coupled CFD-DEM approach in investigating the microscopic mechanism of internal erosion was demonstrated.

As mentioned before, suffusion usually initiates and continues in gap-graded soils under complicated stress states. This process also often involves the rotation of the major principal stress axis and various combinations of the three principal stresses. To better describe the complex stress conditions, the parameter α which presents the angle between the major principal stress and vertical axis and the intermediate principal stress ratio b (given by $[\sigma_2 - \sigma_3]/[\sigma_1 - \sigma_3]$) are introduced in this work. So far, apart from some of the physical tests and simulations which considered some simple stress states, few of the existing studies have investigated the combined effect of α and b due to the difficulty in developing the physical apparatus and numerical CFD-DEM model. In this study, a stress-controlled hollow cylinder torsional shear test (HCTST) DEM model with flexible membrane boundaries allowing for the independent control of α and b is first developed. After the validation work, the seepage flow is introduced. Then, a series of coupled CFD-DEM simulations are conducted for both macroscopic and microscopic investigations of suffusion on gap-graded granular sands under different loading conditions with various α and b.

2 | Methodology

2.1 | Coupled CFD-DEM Method

Three types of formulations are implemented in the CFD-DEM method: the DEM for the solution of the particle system, the framework of CFD for simulating the hydrodynamic process and the CFD-DEM coupling formulation for calculating the fluid-particle interaction forces [18, 24, 29]. In this study, the DEM code PFC3D is used to determine the position, velocity and other quantities of particles by the Newton's laws of motion, and the CFD solver OpenFOAM is used for calculating the pressure gradient, velocity and other quantities of the fluid phase by the averaged Navier–Stokes (N–S) equation. The information exchange between the fluid and particle phases is achieved through the TCP sockets [24, 30].

DEM has been used in many investigations of the microscopic behaviours of granular materials based on the Newton's laws of motion [31, 32]. In DEM, the governing equations of motion of a given particle i at any time t can be expressed in a Lagrangian way as follows:

$$m_i \frac{d\boldsymbol{U}_i}{dt} = \sum_{j=1}^{n_i^c} \boldsymbol{F}_{ij}^c + \boldsymbol{F}_i^f \tag{1}$$

$$I_i \frac{d\omega_i}{dt} = \sum_{j=1}^{n_i^c} \boldsymbol{M}_{ij} \tag{2}$$

where m_i denotes the particle mass; $\boldsymbol{U}_i$ denotes the translational velocity; I_i denotes the moment of inertia tensor; ω_i denotes the angular velocity vector; n_i^c denotes the contact number of the given particle i. $\boldsymbol{F}_{ij}^c$ and $\boldsymbol{M}_{ij}$ are respectively the contact force and torque exerted on the particle i by the surrounding particle j, and the fluid-particle force $\boldsymbol{F}_i^f$ is another force that acts on the particle i.

In the framework of CFD, the information of fluid phase is obtained by solving the locally averaged N–S equation in a Eulerian way. The Lagrangian–Eulerian mapping is introduced to consider the fluid and particle fractions in the discretized fluid elements. The average pressure and velocity at any time t can be solved by the following equations [33]:

$$\frac{\partial n}{\partial t} + \nabla(n\boldsymbol{v}) = 0 \tag{3}$$

$$\rho_f \frac{\partial n\boldsymbol{v}}{\partial t} + \rho_f \boldsymbol{v} \cdot \nabla(n\boldsymbol{v}) = -n\nabla p + \mu\nabla^2(n\boldsymbol{v}) + \boldsymbol{f}_b \tag{4}$$

where n is the local porosity which can account for the effect of the particle phase on the fluid phase; ρ_f is the fluid density; $\boldsymbol{v}$ and p are the average velocity and pressure of the fluid element, respectively; μ is the dynamic viscosity of the fluid. f_b denotes the body force per unit volume exerted on the fluid phase by the particles which localize inside each fluid element, expressed as:

$$\boldsymbol{f}_b = \frac{\sum_{i=1}^{m} \boldsymbol{f}_{fluid}^i}{V} \tag{5}$$

where V is the volume of the fluid element. $\sum_{i=1}^{m} \boldsymbol{f}_{fluid}^i$ is the sum of the particle–fluid interaction forces acting on the particles which overlap the fluid element, and the particle–fluid interaction force $\boldsymbol{f}_{fluid}$ consists of two parts: the drag force and the pressure gradient force:

$$\boldsymbol{f}_{fluid} = \boldsymbol{f}_{drag} + \frac{4}{3}\pi r^3 \left(\nabla p - \rho_f \boldsymbol{g}\right) \tag{6}$$

where $\boldsymbol{g}$ is the gravitational acceleration; r is the particle radius; the term ∇p accounts for the pressure gradient force; and the drag force $\boldsymbol{f}_{drag}$ is expressed as follows:

$$\boldsymbol{f}_{drag} = \boldsymbol{f}_0 n^{-\chi} \tag{7}$$

where $\boldsymbol{f}_0$ denotes the single particle drag force [34], defined as:

$$\boldsymbol{f}_0 = \frac{1}{2} C_d \rho_f \pi r^2 \left|\boldsymbol{u} - \boldsymbol{v}\right| \left(\boldsymbol{u} - \boldsymbol{v}\right) \tag{8}$$

where C_d is the drag coefficient, expressed as:

$$C_d = \left(0.63 + \frac{4.8}{\sqrt{Re_p}}\right)^2 \tag{9}$$

The term $n^{-\chi}$ is an empirical term that accounts for the local porosity of the fluid element, and the coefficient χ is given as follows:

$$\chi = 3.7 - 0.65 \exp\left[-\frac{\left(1.5 - \lg Re_p\right)^2}{2}\right] \tag{10}$$

where Re_p is the Reynolds number of the particles, defined as:

$$Re_p = \frac{2\rho_f r \left|\boldsymbol{u} - \boldsymbol{v}\right|}{\mu} \tag{11}$$

where $\boldsymbol{u}$ is the particle velocity.

In the two-way CFD-DEM coupling algorithm, the following operation sequence is performed. The particle system and the fluid field are first generated according to the designed simulation program. The fluid mesh information is then sent to the DEM part, and the CFD module is initialized in DEM. After the initial calculation of the porosity and drag force, the CFD solver will update the information including the velocity, pressure and pressure gradient of the fluid phase based on the data obtained from DEM, and the updated information will be sent to the DEM part. Then, the DEM solver will cycle forward a time increment which is same as the coupling interval. During the interval, the information of the particle system is updated, and the fluid-particle interaction force will be added to the particles. The above steps will be repeated until the required coupling time.

2.2 | Validation of the Coupled CFD-DEM Method

Many tests including the drop test [24, 30], sedimentation test [27], Ergun test [11, 23] and fluidization test [28] have been used to validate the coupled CFD-DEM method. In this study, the Ergun test is conducted for the benchmarking [35]. During the test, there is a pressure drop ∇p between the inlet and outlet of the CFD domain (Figure 1), and the analytical solution of the pressure drop

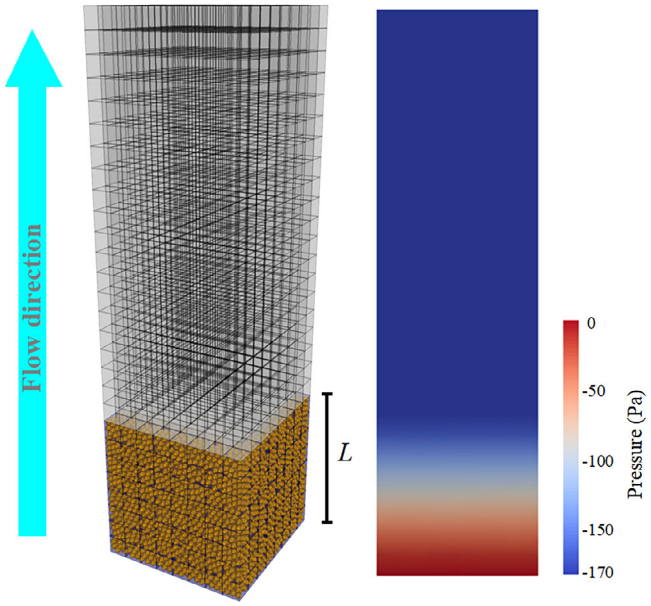

FIGURE 1 | The coupled CFD-DEM model for the Ergun test.

can be described by the following expression:

$$\nabla p = \frac{150\mu L(1-e)^2}{d^2 e^3}\boldsymbol{v}_s + \frac{1.75 L\rho(1-e)}{de^3}\boldsymbol{v}_s\left|\boldsymbol{v}_s\right| \tag{12}$$

where L denotes the particle bed height; d is the particle diameter; $e = 0.47$ is the initial void ratio of the particle assembly. The fluid density ρ and dynamic viscosity μ are set as 1000 kg/m^3 and 1.5×10^{-3} Pa, respectively.

In the benchmarking simulation, a particle bed with the size of 15.6 × 15.6 × 15.6 mm is first generated. The particles with the same diameter of 0.65 mm are connected by the linear elastic contact model, and the elastic modulus, stiffness ratio and friction coefficient are 1.0×10^8 Pa, 3.0 and 0.3, respectively. Then, a CFD domain with the size of 15.6 × 15.6 × 62.4 mm is introduced to achieve the flow of fluid through the particle assembly from bottom to top at a different superficial velocity $\boldsymbol{v}_s$.

Different pressure drop magnitudes are obtained with various superficial velocities from the coupled CFD-DEM simulation (Figure 2). The good agreement between the numerical result and analytical solution indicates that the CFD-DEM method can well capture the interaction behaviour between the particle and fluid phases. More benchmarking work can be found in our previous work [24].

2.3 | DEM HCTST Model

As a widely used tool in geotechnical research, hollow cylinder apparatus (HCA) can help to independently control the stress components (the vertical stress σ_z, torsional shear stress $\tau_{z\theta}$, circumferential stress σ_θ and radial stress σ_r) by adjusting the external loads (the vertical load W, torque T, internal cell pressure p_i and external cell pressure p_o) in real time. The formulae used to calculate the stress and corresponding strain components are summarized in Table 1.

TABLE 1 | Equations used to calculate the stresses and strains in the HCTST.

Vertical	$\sigma_z = \frac{W}{\pi(r_o^2 - r_i^2)}$	$\varepsilon_z = \frac{z}{H}$
Radial	$\sigma_r = \frac{p_o r_o + p_i r_i}{r_o + r_i}$	$\varepsilon_r = -\frac{\mu_o - \mu_i}{r_o - r_i}$
Circumferential	$\sigma_\theta = \frac{p_o r_o - p_i r_i}{r_o - r_i}$	$\varepsilon_\theta = -\frac{\mu_o + \mu_i}{r_o + r_i}$
Torsional	$\tau_{z\theta} = \frac{3T}{2\pi(r_o^3 - r_i^3)}$	$\gamma_{z\theta} = \frac{\theta}{3H(r_o^2 - r_i^2)}$
Major principal	$\sigma_1 = \frac{\sigma_z + \sigma_\theta}{2} + \sqrt{\left(\frac{\sigma_z + \sigma_\theta}{2}\right)^2 + \tau_{z\theta}^2}$	$\varepsilon_1 = \frac{\varepsilon_z + \varepsilon_\theta}{2} + \sqrt{\left(\frac{\varepsilon_z + \varepsilon_\theta}{2}\right)^2 + \gamma_{z\theta}^2}$
Intermediate principal	$\sigma_2 = \sigma_r$	$\varepsilon_2 = \varepsilon_r$
Minor principal	$\sigma_3 = \frac{\sigma_z + \sigma_\theta}{2} - \sqrt{\left(\frac{\sigma_z + \sigma_\theta}{2}\right)^2 + \tau_{z\theta}^2}$	$\varepsilon_3 = \frac{\varepsilon_z + \varepsilon_\theta}{2} - \sqrt{\left(\frac{\varepsilon_z + \varepsilon_\theta}{2}\right)^2 + \gamma_{z\theta}^2}$

Note: ε_z, ε_r, ε_θ and $\varepsilon_{z\theta}$ are the vertical, radial, circumferential and torsional shear strain components, respectively; z, θ, μ_o and μ_i are the vertical, angular circumferential, outer and inner radial displacements, respectively; H, r_o, and r_i are the initial height, outer and inner radii of the HCTST specimen, respectively.
Abbreviation: HCTST, hollow cylinder torsional shear test.

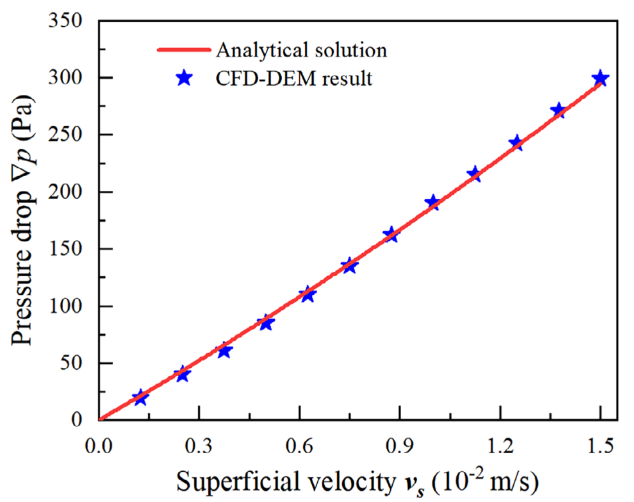

FIGURE 2 | Comparison between the analytical solution and the CFD-DEM simulation result of the Ergun test.

Furthermore, to better understand the stress states in HCTSTs, the following equations are used to describe the stress states in the stress space of mean normal stress p and deviatoric stress q [36, 37]:

$$\sigma_z = p - \frac{1}{3}q\left(b - \frac{1}{2}\right) + \frac{1}{2}q\cos(2\alpha) \tag{13}$$

$$\sigma_r = p + \frac{2}{3}q\left(b - \frac{1}{2}\right) \tag{14}$$

$$\sigma_\theta = p - \frac{1}{3}q\left(b - \frac{1}{2}\right) - \frac{1}{2}q\cos(2\alpha) \tag{15}$$

$$\tau_{z\theta} = \frac{1}{2}q\sin(2\alpha) \tag{16}$$

Therefore, many loading conditions with various of α and b can be achieved by combining the two sets of stress states and adjusting the corresponding external loads in HCTSTs. More details about the principle of HCTST can be found in previous studies [36–40].

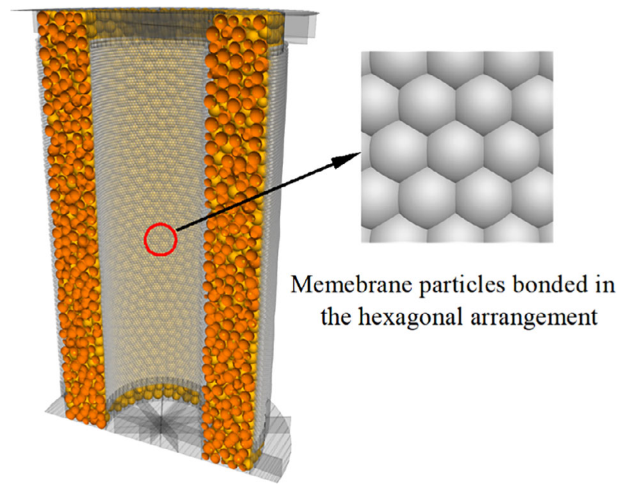

FIGURE 3 | DEM HCTST model and the flexible membrane boundary.

Based on the above principle, a DEM HCTST model is proposed in this study, as shown in Figure 3, to achieve the simulations under various stress conditions. In this model, the top plate moves up and down to achieve the adjustment of the vertical load, and the torque is applied on the DEM specimen trough the rotation of the top short vertical plates. The real-time adjustments of the internal and external cell pressures are achieved by applying forces on the sphere elements of the flexible membrane boundaries. The inner and outer flexible membrane boundaries used in this study are made of sphere elements bonded in a hexagonal arrangement, and each sphere element can be regarded as a central node (Figure 3). The force applied on the central node is determined based on the surrounding sphere elements, and it is continuously updated according to the pre-determined pressure and the positions of these spheres during the simulation. The flexible membrane is generated following the steps: (a) generate the particle assembly in the HCA mould with rigid walls; (b) determine the positions of the nodes and generate the bonded flexible membrane spheres to surround both the inner and outer rigid walls; (c) delete the inner and outer rigid boundaries; (d) apply forces to the membrane sphere elements. It is noted that

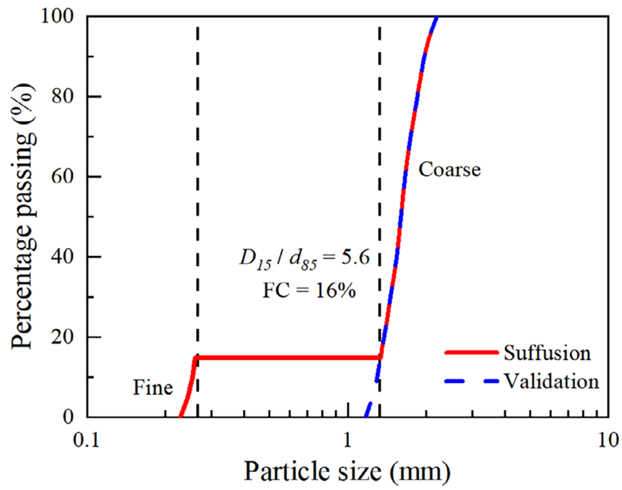

FIGURE 4 | Particle size distribution used in the validation and suffusion simulations.

different contact models are used to capture the interactions among different materials in this model: the linear parallel bond contact model is selected to bond the membrane elements (MM), the rolling resistance linear model is used to capture the interactions between granular particles (PP), and the linear elastic contact model is used to describe the interactions between particle and wall (PW), particle and membrane (PM), as well as membrane and wall (MW). Similar flexible boundary algorithms have been previously demonstrated to accurately capture the mechanical characteristics of the real membrane used in physical tests [37, 41–43].

2.4 | Validation of the DEM HCTST Model

The HCTST simulation with the fixed major principal stress direction ($\alpha = 60°$) and intermediate principal stress ratio ($b = 0.5$) is conducted for the validation work of the proposed DEM HCTST model. This DEM specimen has a size of 30 and 50 mm in the inner and outer diameters, respectively, and the height is twice the outer diameter. It is noted that the mean normal stress p is also kept unchanged at 98 kPa during the shearing process, and more details about the test can be found in the experimental study by Miura et al. [44] The PSD used in the validation is shown in Figure 4 (the blue dashed line). Figure 5 presents the comparison between the numerical simulation and experimental results. The good agreements in both stress and strain components demonstrate the ability of the proposed DEM HCTST model in the description of the mechanical behaviour of granular materials in the HCTSTs.

More validation work can be found in our previous study [37]. It is noted that the parameters related to the flexible membrane boundaries have been determined before shearing with the same method as the one in Zhang et al. [45]. In short, tensile and suspension simulation tests are performed to determine the effective modulus E_{PP}, normal bond stiffness $\bar{k}_n$, tangential bond stiffness $\bar{k}_s$ and other related parameters. Meanwhile, a series of sliding tests are conducted to determine the friction coefficients between the membrane spheres, the soil particles and the rigid walls. These parameters and the calibrated parameters related to soil particles used in the validation are listed in Table 2, and they will be also used in the following coupled CFD-DEM simulations of suffusion under various loading conditions considering different values of both α and b.

TABLE 2 | Parameters used in the coupled CFD-DEM simulations.

Parameters			Values
DEM	Elastic modulus	E_{PP} (Pa)	2.0×10^8
		E_{PW} (Pa)	2.0×10^8
		E_{PM} (Pa)	2.0×10^6
		E_{MM}(Pa)	1.00×10^6
		E_{MW}(Pa)	1.00×10^6
	Stiffness ratio	k_{PP}	3.0
		k_{PW}	3.0
		k_{PM}	3.5
		k_{MM}	3.0
		k_{MW}	4.0
	Friction coefficient	μ_{PP}	0.30
		μ_{PW}	0.20
		μ_{PM}	0.35
		μ_{MM}	0.90
		μ_{MW}	0.65
	Rolling friction coefficient	μ_r	0.1
	Normal stiffness of the linear parallel bond	$\bar{k}_n$ (Pa/m)	3.0×10^8
	Tangential stiffness of the linear parallel bond	$\bar{k}_s$ (Pa/m)	1.00×10^8
	Density of particles	ρ_p (kg/m^3)	2650
	Density of membrane particles	ρ_m (kg/m^3)	809
CFD	Cells	Radial × circumferential × vertical directions	$3 \times 12 \times 25$
	Fluid viscosity	μ (Pa*s)	1.0×10^3
	Density of fluid	ρ_f (kg/m^3)	1000

Abbreviations: CFD, computational fluid dynamics; DEM, discrete element method.

3 | Simulation Program

Based on the DEM HCTST model, nine suffusion simulations are designed with different α and b, as summarized in Table 3. As the main objective of this study is to investigate the suffusion under different loading conditions, the variation of FC is not considered, and all suffusion cases have the same FC of 16%. Previous studies found that the granular soil is internally unstable when the gap ratio $D_{15}/d_{85} > 4$ (where D_{15} and d_{85} represent the particle diameters of 15% mass passing in the coarse particles and

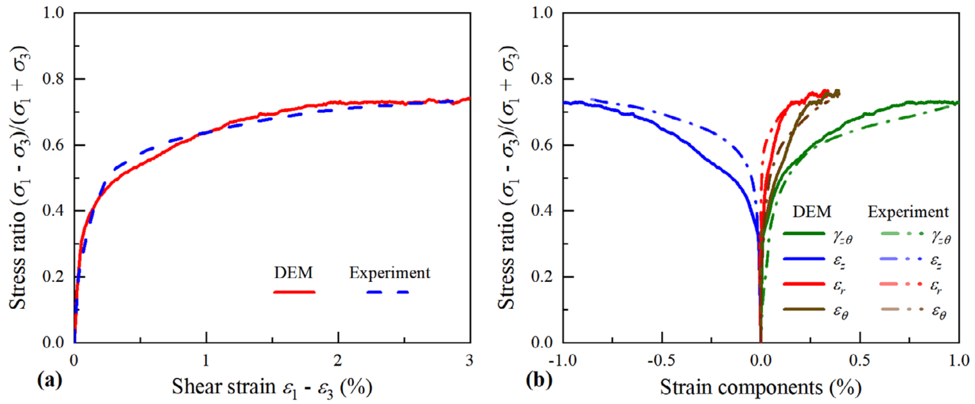

FIGURE 5 | Comparison between the experimental and numerical results: (a) Stress ratio; (b) Strain components.

TABLE 3 | Simulation program.

Test	1	2	3	4	5	6	7	8	9
α	25°	25°	25°	45°	45°	45°	65°	65°	65°
b	0.2	0.5	0.8	0.2	0.5	0.8	0.2	0.5	0.8

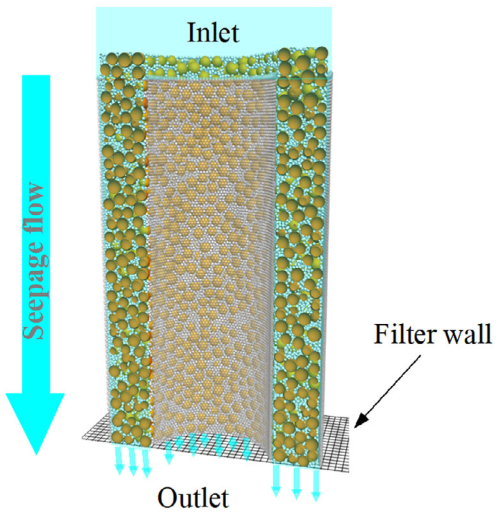

FIGURE 6 | The coupled CFD-DEM suffusion model.

85% mass passing in the fine particles, respectively) [46, 47]. Thus, the gap ratio of the gap-graded soil is set as 5.6 in this paper, as shown in the PSD curve (the red solid line in Figure 4).

The HCTST specimen used in the coupling simulation matches the size of the DEM model used in the validation process. Before coupling, the specimen is first generated with a relative density D_r ($=[e_{max}—e]/[e_{max}—e_{min}]$) of around 64.3%. The specimen is then sheared under different loading paths with various fixed α and b, and the confining pressure p is kept constant at 50 kPa during the whole shearing process. When the deviatoric stress q reaches 55 kPa, the shearing process is paused, and the CFD domain is then introduced for the suffusion simulations. Meanwhile, the bottom rigid boundary is replaced by a filter wall with holes whose size is about 2.5 times the diameter of the largest fine particles but smaller than that of the coarse particles (Figure 6), so that the fine particles can be washed out of the specimen by the fluid flow. The stress states of the nine cases are kept the same except for the major principal stress direction and intermediate principal stress ratio during the suffusion process. In addition, the shearing will restart to adjust the stress components if the stress states of the specimens have deviated from the pre-determined values due to the seepage flow and loss of the fine particles.

The introduced CFD domain has the same inner and outer diameters as the particle assembly, while the height is set as 1.5 times that of the DEM sample. The free slip boundary condition is applied on both the inner and outer lateral CFD boundaries, and the fluid flows from top to bottom by applying the fluid pressures at the inlet and outlet boundaries. The hydraulic gradient i ($=\Delta p/\rho gL$, where Δp denotes the differential pressure between the inlet and outlet boundaries, and L denotes the length of the particle assembly along the flow direction) is set as 2.0 in this study. The coupling simulation process lasts for 10 s in all cases. It is noted that the Courant number C, expressed in the following equation, should be below 1 during the whole suffusion process: [48]

$$C = \frac{\sum_F U_F \Delta S}{2\Delta V}\Delta t_f < 1 \tag{17}$$

where $\sum_F U_F \Delta S$ is the sum of the face fluxes of a fluid element; ΔV is the volume of the fluid element; and Δt_f denotes the timestep in the CFD calculation. Meanwhile, the timestep Δt_p in the DEM domain should satisfy the criteria proposed by Cundall and Strack [49]:

$$\Delta t_p \le 2\sqrt{\frac{M}{k}} \tag{18}$$

where M and k are the particle mass and stiffness, respectively. In this study, Δt_p is approximately 1×10^{-7} s, and Δt_f is set as 1×10^{-5} s. More parameters used in the suffusion simulations are summarized in Table 2.

4 | Result Analysis

4.1 | Mass Loss of Fine Particles

Figure 7 shows the cumulative mass loss of fine particles during suffusion and the ultimate values in the nine cases having

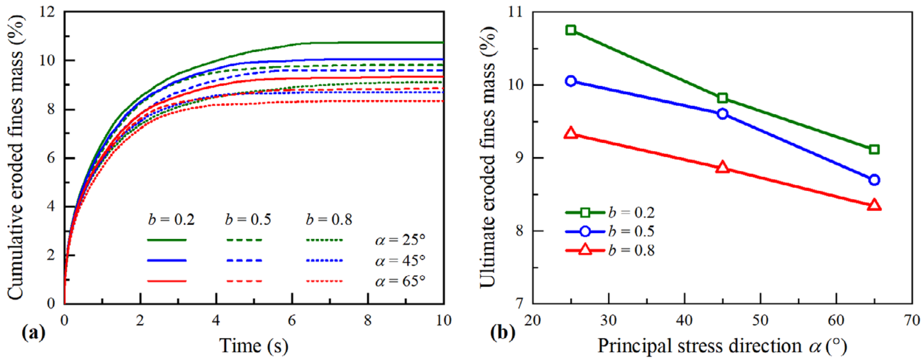

FIGURE 7 | (a) Cumulative eroded fines mass during suffusion and (b) the ultimate values for cases with different α and b.

different α and b. It is concluded that the cases with smaller α have more fine particles eroded. In other words, as the major principal stress gradually rotates from the vertical direction to the horizontal direction, fewer fine particles are washed away by the fluid flow. Meanwhile, the fines mass loss is also influenced by the value of b. In detail, more fine particles are eroded in the cases having smaller b under otherwise same loading conditions, which is consistent with the observation in Liu et al. [50]. The differences of the fines mass loss in cases having different α and b can be explained by the stress-controlled HCTST loading system. In short, the circumferential stress σ_θ whose direction is perpendicular to the fluid flow increases with α, and another applied stress perpendicular to the vertical direction, the radial stress σ_r, increases as b increases [39]. Therefore, the restriction on the particles on the horizontal plane is more significant in cases having larger α and b, resulting in the largest cumulative eroded fines mass (10.8%) observed in the case with $\alpha = 25°$ and $b = 0.2$, while the fines mass loss (8.3%) is the smallest when $\alpha = 65°$ and $b = 0.8$. The microscopic explanations for the macroscopic difference in the fines mass loss are given in the following sections.

With the applied hydraulic gradient, the fine particles are not transported uniformly through the pores due to the restriction by the clogging, applied stress and other factors [22, 28, 51]. The DEM specimen is divided into nine equal layers along the vertical direction, as shown in Figure 8, to facilitate the investigation of the fines mass loss under different loading conditions. The cases with $b = 0.2$ and having $\alpha = 65°$ are taken as examples here. The distributions of the particle numbers in the nine layers before and after erosion are plotted in Figure 9. In general, most fine particles are eroded in Layer 1 which is near the filter wall in all cases, and the loss of fine particles in Layer 9 is also significant. By contrast, the variations of the particle numbers in middle layers are much smaller, which is consistent with Liu et al. [27] and Zhou et al. [28]. The possible explanation for this phenomenon is that the clogging in middle layers has restricted the movement of fine particles from top to bottom. To have a clearer understanding, three coarse particles and the surrounding connected fine particles in Layer 5 at $t = 0$ s and 6 s are shown in Figure 9. In comparison with the initial state, some fine particles are observed to be blocked in the pore between the coarse particles at the moment $t = 6$s, resulting in other fine particles not being able to migrate downward through this pore after the clogging occurs [22]. Meanwhile, the distribution of particle numbers along the vertical direction is affected by both α

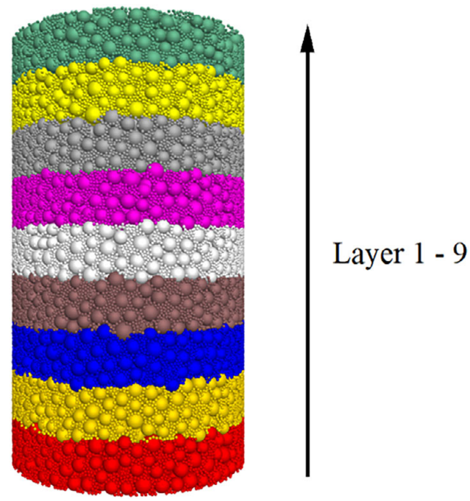

FIGURE 8 | Classified layers of the DEM sample along the vertical direction.

and b. As α increases from 25° to 65°, more particles are observed in the middle layers after erosion. Similarly, more fine particles are blocked in the middle layers with the increase of b. This can be also explained by the aforementioned different applied stress components in cases having various α and b: the increased restriction from the direction perpendicular to the fluid flow with the increases of both α and b results in more significant clogging in the middle layers, especially in Layers 4 and 5 where there are more particles after erosion than the initial state.

4.2 | Volume Flow Rate

There is a strong mutual influence between the fluid phase and particle system during the process of suffusion. Thus, the behaviour of fluid phase should be also considered. The evolutions of the volume flow rate Q ($=\boldsymbol{v} \cdot A$, where A is defined as the area of the ring in the middle of Layer 2 in this study; the flow velocity $\boldsymbol{v}$ is defined as $\boldsymbol{v} = \boldsymbol{k} \cdot i$, and $\boldsymbol{k}$ is the hydraulic conductivity) in cases under different loading conditions are shown in Figure 10. It is concluded that the volume flow rates all increase during the suffusion process despite the different loading conditions. The smallest rates in all cases are observed at the moment $t = 0$ s, indicating that fines mass loss can increase the hydraulic conductivity $\boldsymbol{k}$ of the HCTST specimens. In addition, the increasement of permeability decreases with the increases

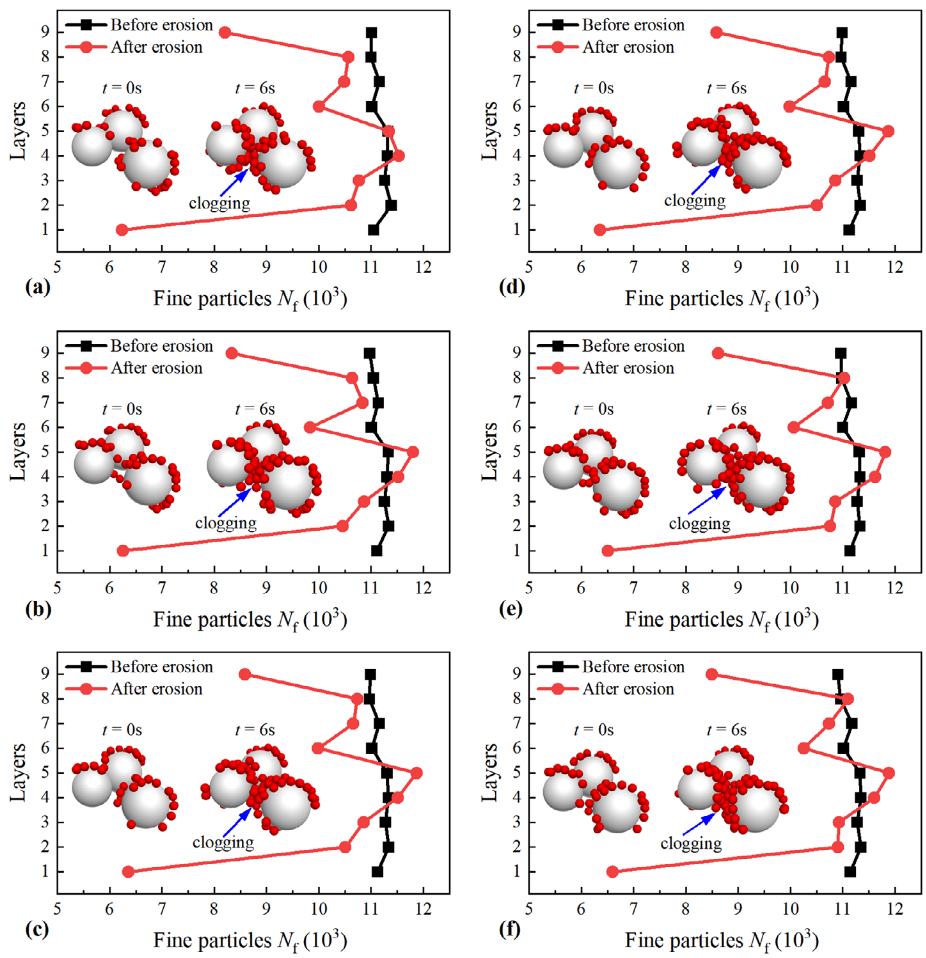

FIGURE 9 | Distribution of particle numbers in layers for cases: (a–c) $b = 0.2$ with $\alpha = 25°$, $45°$ and $65°$, respectively; (d–f) $\alpha = 65°$ with $b = 0.2$, 0.5 and 0.8, respectively.

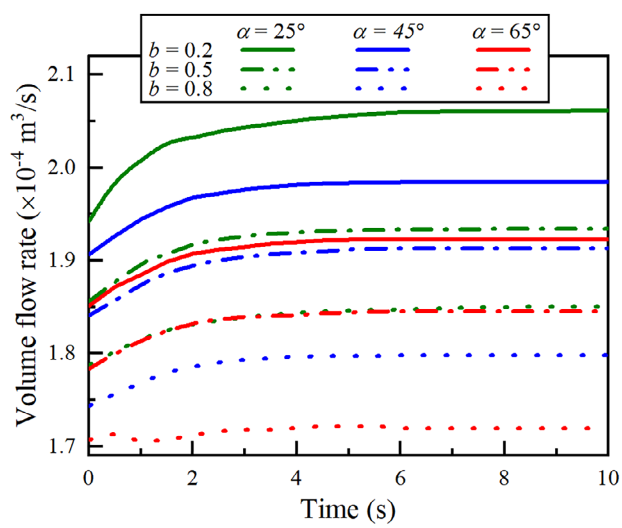

FIGURE 10 | Evolution of the volume flow rate for all cases.

of both α and b. The greatest value of the volume flow rate is observed in the case having $\alpha = 25°$ and $b = 0.2$, while the permeability is the smallest in the case with $\alpha = 65°$ and $b = 0.8$. In other words, the more the fines mass loss, and the greater the volume flow rate.

4.3 | Strong Force Chains

The force transmission and contact anisotropy are mainly contributed by the strong force chains in the granular packing, while the weak ones are mainly responsible for the maintenance of the stability of the strong force chains [11, 52]. For the gap-graded materials, Liu et al. [27] further found that the fine particles with higher contact forces and connectivity are more difficult to be washed away by the fluid flow. To facilitate the investigation of the contributions of particles with different sizes to the strong force chains, three types of contacts are categorized in this study: the contact between coarse particles (*c-c* contact), the contact between fine particles (*f-f* contact) and the contact between coarse and fine particles (*c-f* contact) [11, 28]. The cut-off point between the strong and weak forces is set as the average contact force f_a here [27, 53], defined as:

$$f_a = \frac{\sum_{N_c} f_i}{N_c} \tag{19}$$

where N_c is the total number of contacts and f_i is the contact force at a contact. The forces which are greater than f_a are the strong contact forces, while the ones less than f_a are defined as the weak contact forces. In addition, the proportion P_s which denotes the percentage of strong force chains in different types of contacts to

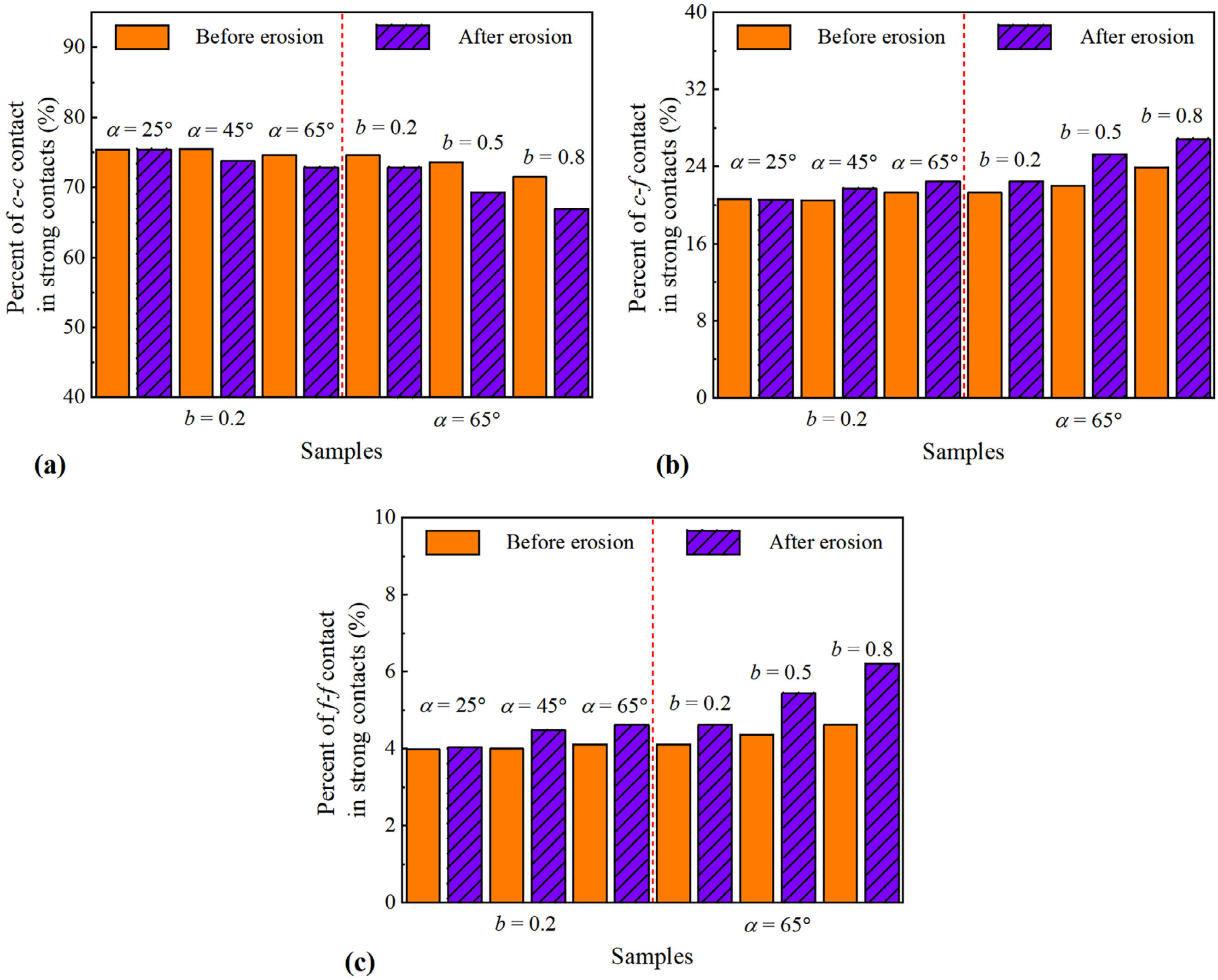

FIGURE 11 | Contributions of (a) *c-c*, (b) *c-f* and (c) *f-f* contacts to the strong force chain network before and after erosion.

the total strong force chains can be calculated by the following equation:

$$P_s = \frac{N_s^{ct}}{N_s} \tag{20}$$

where N_s^{ct} is the number of strong force chains in each contact type and N_s is the number of total strong chains.

Figure 11 shows the contributions of the three types of contacts to the strong force chain network for the same cases as those in Figure 9 before and after erosion. In general, the type of *c-c* contact plays a dominant role in both pre-eroded and post-eroded particle assemblies in all cases, while the type of *f-f* contact accounts for the smallest proportion. On the other hand, fine particles have made more contributions to the strong force chains after the suffusion process, proved by the increases of the percents of the *c-f* and *f-f* contacts (Figure 11b,c). This phenomenon can be attributed to the fact that some of fine particles are clogged in the pores between coarse particles and may overfill the pores during the suffusion process. These fine particles will then bear greater contact forces, [27] which further makes it more difficult for fine particles to be washed away.

The percents of the *c-f* and *f-f* contacts in strong force chains in layers of these post-eroded samples are plotted in Figures 12 and 13 for further analysis. In general, fine particles are found to contribute more to the strong force chains in the middle layers, which is consistent with the particle number distribution shown in Figure 9. This means that some of the fine particles moved from the upper layers have overfilled the pores and been obstructed in the middle layers, further bearing greater loads. Meanwhile, the percents of the two types of contacts related to fine particles increase with both α and b in most layers, implying that more fine particles are strongly connected with other surrounding particles, and less fine particles are washed away as both α and b increase.

4.4 | Anisotropy of Contact Force and Force Chain Network

To have a deep understanding of the differences in suffusion under various loading conditions, the spatial distribution of the microscopic contact orientation is considered in this study [9, 23, 28]. The distribution function which can quantify the

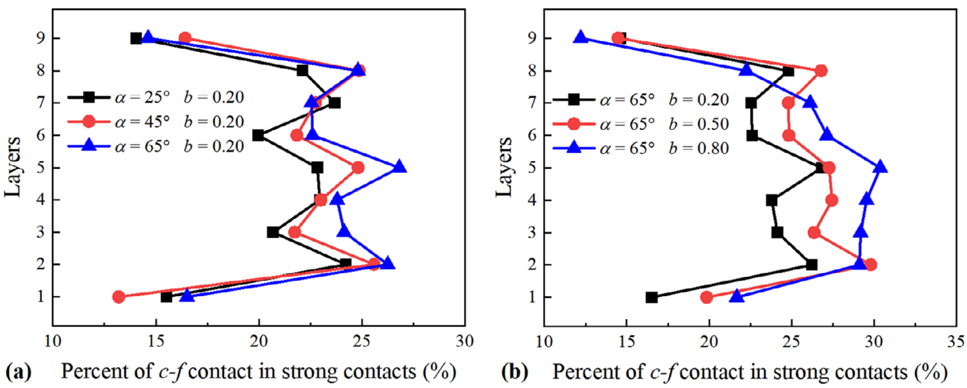

FIGURE 12 | Percent of *c-f* contact in the strong contacts in layers for cases: (a) b = 0.2 with $\alpha = 25°$, 45° and 65°, respectively; (b) $\alpha = 65°$ with b = 0.2, 0.5 and 0.8, respectively.

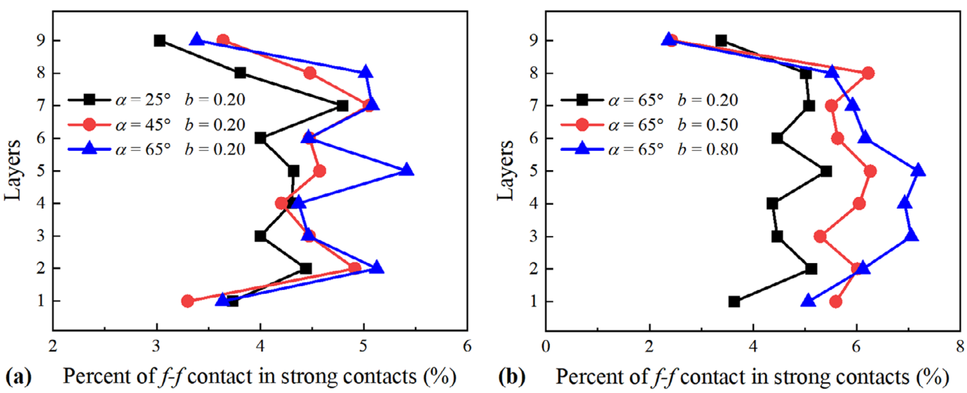

FIGURE 13 | Percent of *f-f* contact in the strong contacts in layers for cases: (a) b = 0.2 with $\alpha = 25°$, 45° and 65°, respectively; (b) $\alpha = 65°$ with b = 0.2, 0.5 and 0.8, respectively.

contact information can be defined by the following Fourier series:

$$E(\varphi) = \frac{1}{2\pi}\left[1 + \mathrm{A}\cos(\varphi - \mathrm{B})\right] \tag{21}$$

where φ denotes the angle between the directions of the contact and vertical axis; A and B are the magnitude and the corresponding principal direction of the anisotropy, respectively, and they can be calculated by the following equations [11, 23]:

$$\mathrm{A} = 2\sqrt{\left[\int_0^{2\pi} E(\varphi)\cos 2\varphi d\varphi\right]^2 + \left[\int_0^{2\pi} E(\varphi)\sin 2\varphi d\varphi\right]^2} \tag{22}$$

$$\mathrm{B} = \frac{1}{2}\arctan\frac{\int_0^{2\pi} E(\varphi)\sin 2\varphi d\varphi}{\int_0^{2\pi} E(\varphi)\cos 2\varphi d\varphi} \tag{23}$$

Figures 14 and 15 show the spatial distributions of normal contact force and contact normal for three cases before and after suffusion. After suffusion, the principal directions of both normal contact force and contact normal rotate slightly to the vertical direction in the three cases, and more contacts are generated along the vertical direction due to the seepage flow. Meanwhile, the specimens with $\alpha = 45°$ and 65° tend to be less anisotropic with the decreased anisotropy magnitudes, while the anisotropy magnitude of the sample with $\alpha = 25°$ shows a slight increase. To have a better understanding, the evolutions of the two anisotropy parameters of both normal contact force (A_n and B_n) and contact normal (A_c and B_c) for all cases during the suffusion process are plotted in Figures 16 and 17. In general, the applied fluid flow is observed to be able to reduce the anisotropy levels although constant anisotropic stresses are continually imposed on the specimens in cases with $\alpha = 45°$ and 65°. For cases with $\alpha = 25°$, the anisotropy magnitudes also decrease although there is a slight increase during the initial seconds. The slightly decreased anisotropy magnitudes and the corresponding directions which are slightly rotating to the fluid direction suggest that some contacts along the major principal stress directions are destroyed, and some new contacts are generated along the vertical direction under the action of fluid flow. Furthermore, the possible explanation of the initial increase in magnitude in cases with $\alpha = 25°$ is that the contacts in the horizontal plane are not as strong as those in the cases where $\alpha = 45°$ and 65° due to the smaller circumferential stress σ_θ, [39] and some of the horizontal contacts are easier to be destroyed in the initial stage. The free particles are then quickly connected with the surrounding particles along the flow direction which is close to the initial principal direction of anisotropy. Thus, the anisotropy principal directions rotate to the vertical direction quickly, and the specimens become more anisotropic at the initial stage. Like the cases with $\alpha = 45°$ and 65°, some of the contacts along the anisotropy principal direction break during the following suffusion process, and the magnitudes begin to decrease.

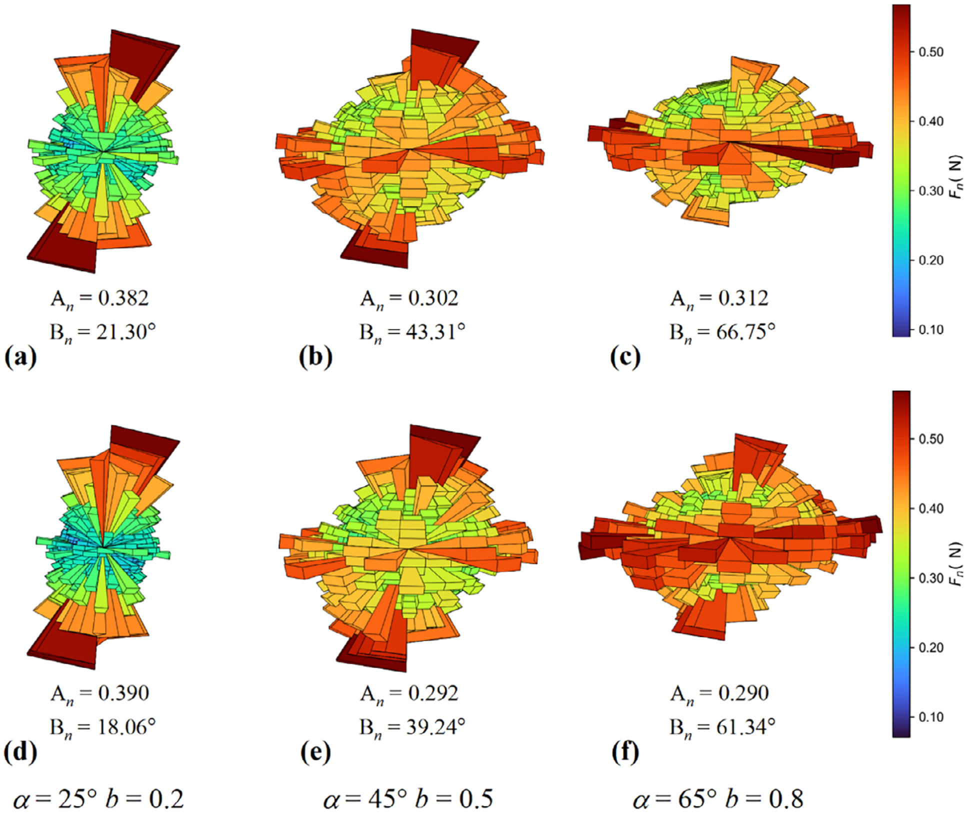

FIGURE 14 | Distribution of normal contact force (a–c) before and (d–f) after suffusion for cases: $\alpha = 25°$ and $b = 0.2$ (left column); $\alpha = 45°$ and $b = 0.5$ (mid column) and $\alpha = 65°$ and $b = 0.8$ (right column).

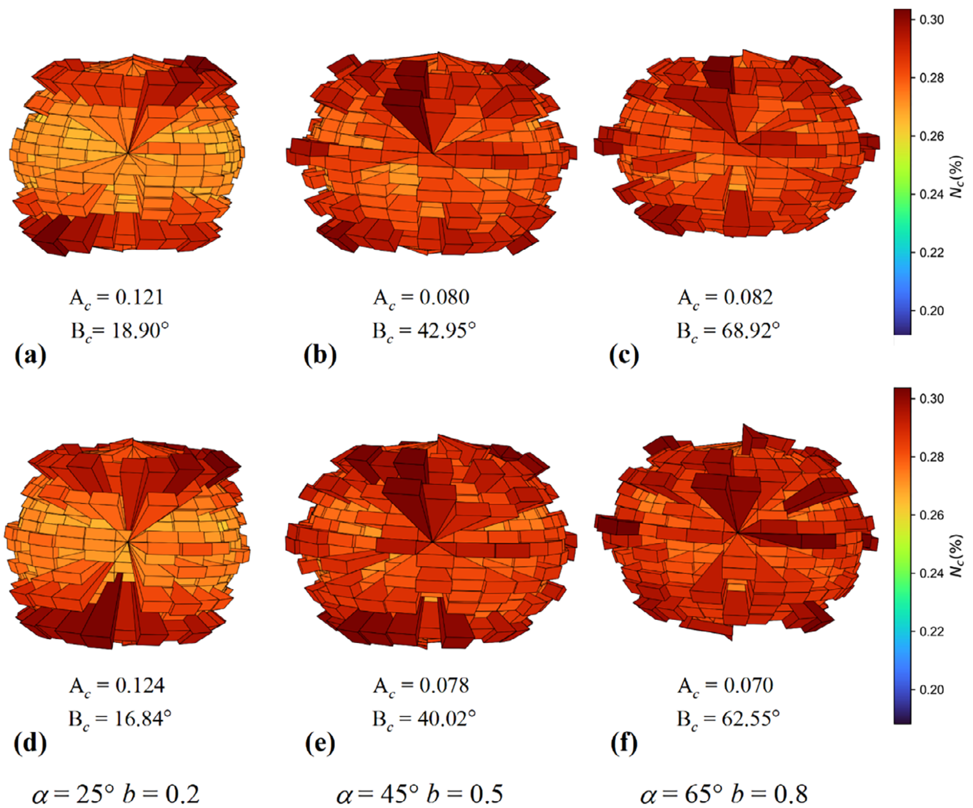

FIGURE 15 | Distribution of contact normal (a–c) before and (d–f) after suffusion for cases: $\alpha = 25°$ and $b = 0.2$ (left column); $\alpha = 45°$ and $b = 0.5$ (mid column) and $\alpha = 65°$ and $b = 0.8$ (right column).

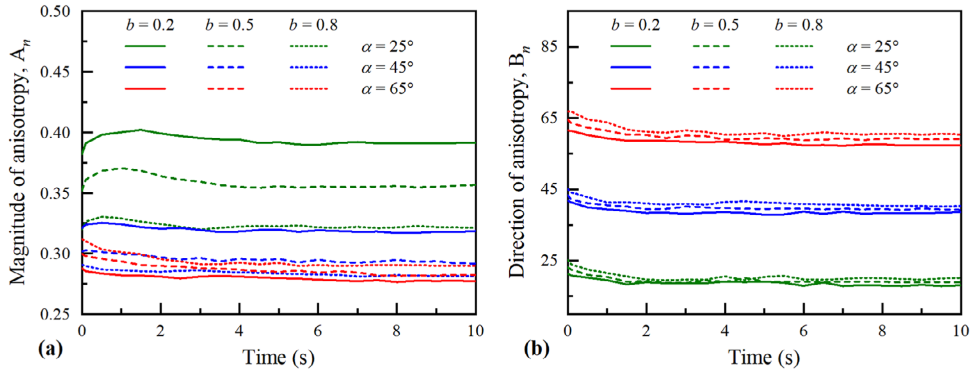

FIGURE 16 | Evolution of the (a) anisotropy magnitude and (b) principal direction of normal contact force during suffusion.

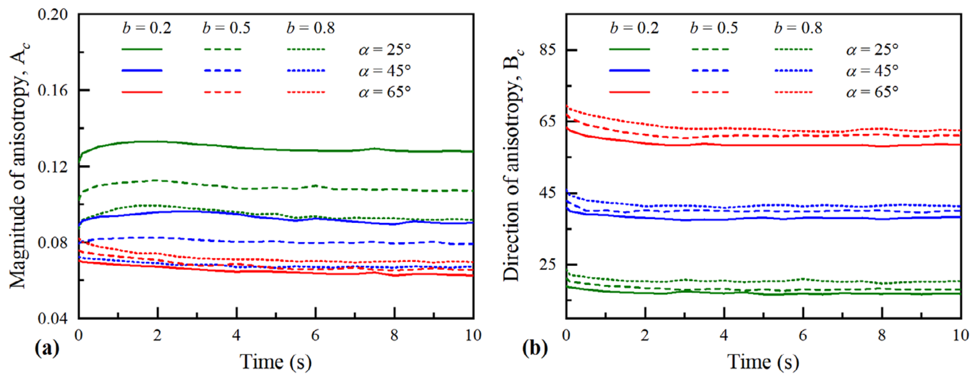

FIGURE 17 | Evolution of the (a) anisotropy magnitude and (b) principal direction of contact normal during suffusion.

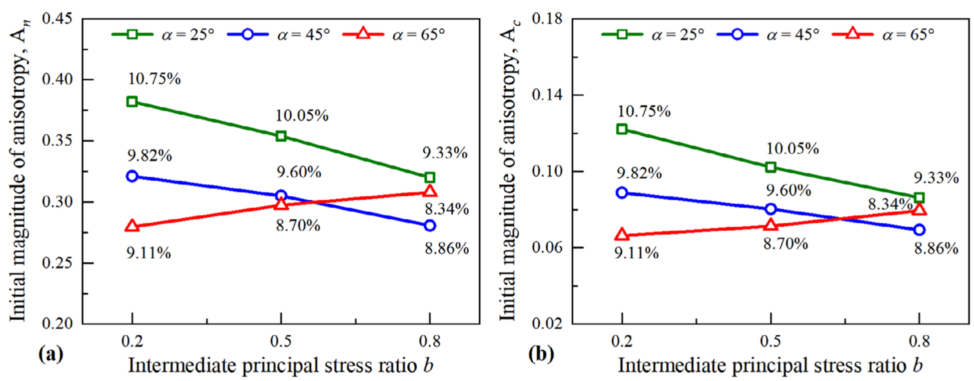

FIGURE 18 | Relationship between the initial anisotropy magnitude and intermediate principal stress ratio: (a) normal contact force, (b) contact normal (the number near the point is the percentage of ultimate fines mass loss).

The anisotropy magnitudes before suffusion show a decreasing trend with b when $\alpha = 25°$ and 45°, while an opposite trend is observed when $\alpha = 65°$, as shown in Figure 18. This can be attributed to the fact that when $\alpha = 65°$, the radial stress σ_r is relatively large. Concurrently, the vertical stress σ_z decreases as b increases. This reduction in σ_z results in a higher number of inherent contacts distributed along the vertical direction breaking, and the generation of new contacts along the horizontal direction in the cases with larger b-values during shearing [36, 37, 39]. On the other hand, although the majority of loads are resisted by the contacts distributed vertically when $\alpha = 25°$ and 45°, more contacts are observed along the horizontal direction due to the increase of the radial stress σ_r with b, resulting in the decrease of the anisotropy magnitude with b. Consequently, it becomes increasingly challenging for fine particles to overcome the horizontal constraints in cases with larger b-values, consistent with the observation in Figure 7. Similarly, for cases having the same b, the more the principal direction deviates from the fluid (vertical), the higher restriction from the horizontal direction, and the fewer the fines mass loss. More information about the contact distribution can be seen in the force chain network analysis in Figure 19.

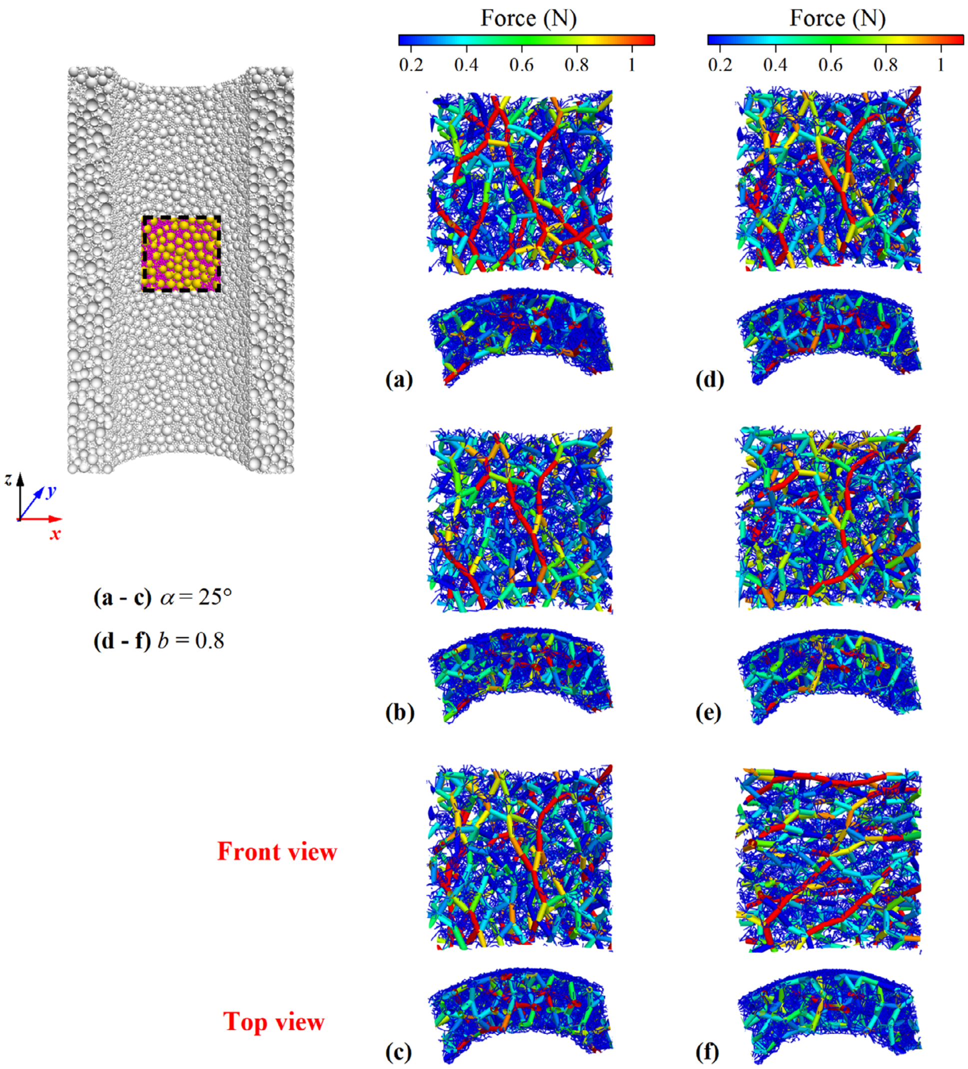

FIGURE 19 | Local contact force networks for cases: (a–c) $\alpha = 25°$ with $b = 0.2$, 0.5 and 0.8, respectively; (d–f) $b = 0.2$ with $\alpha = 25°$, 45° and 65°, respectively.

Local contact force networks (the zone highlighted by the red dashed line) of some cases are shown in Figure 19 for the microscopic analysis. From the front views, the stress anisotropy is clearly captured by the force chains which are gradually rotating to be close to the horizontal direction as α increases from 25° to 65° (Figure 19d–f), consistent with Figures 16 and 17. Meanwhile, more strong force chains are observed in the horizontal plane from the top views due to the increased restriction by the radial stress σ_r with the increase of b (Figure 19a–c).

4.5 | Pore Structure and Erosion Path

For the specimens under different loading conditions, the internal particles undergo rotation and sliding during the shearing process, and the contacts between particles exhibit varying degrees of buckling and collapse [37, 54]. In other words, the internal structures of these granular systems undergo varying degrees of change, and correspondingly, the pores between the particles have also exhibit differences. To describe the pore structures of the particle assemblies, the maximal ball (MB) method which can be used to extract pore networks from generic and arbitrary 3D images is introduced. [55] With this method, Silin et al. [56] and Silin and Patzek [57] studied the dimensionless capillary pressure during drainage processes. Xiong et al. [22] investigated the pore structure of porous media, further analysing the effect of pore size on the degree and position of clogging. In this study, the HCTST specimen is first divided into many voxels. Then, the MB method operates by finding the largest inscribed ball at each voxel coordinate whose radius is equivalent to the minimal distance to the particle phase or boundaries. [22] Then, the balls that are included in the largest inscribed balls are regarded as inclusions and are removed. The rest, referred to as the maximal balls, provide a non-redundant representation of the pore space. The MB clusters are then extracted and plotted to outline the porous skeletons, thereby offering a depiction of the attributes of pores. More details about the MB method can be found in previous studies [55, 57, 58].

Figure 20 shows the local pore structures of some cases, and the local zone is the same as that in Figure 19. Compared to the case with $\alpha = 25°$ and $b = 0.2$, the pores in the specimen having

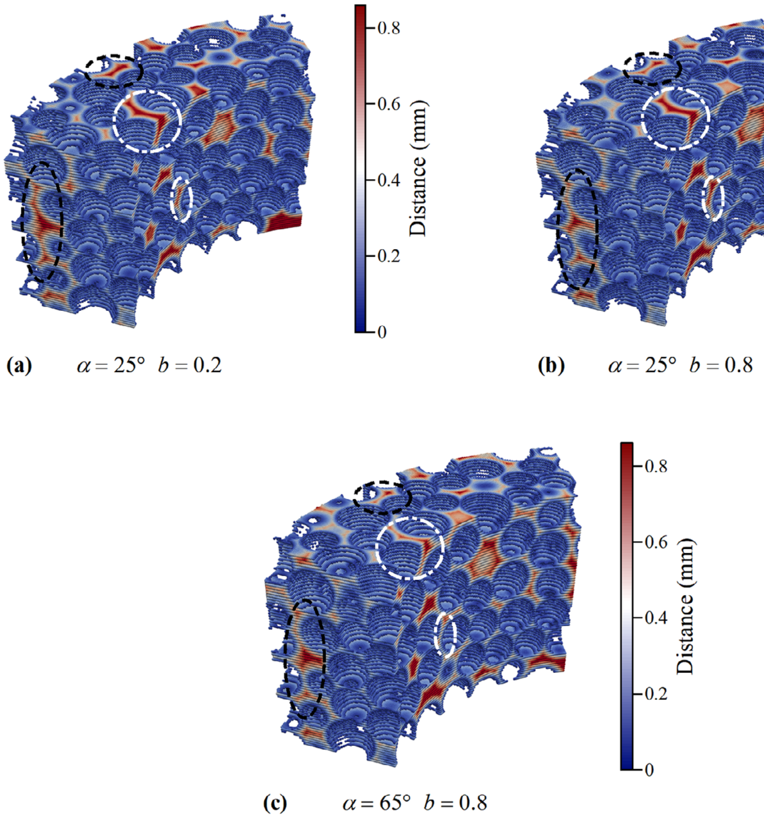

FIGURE 20 | Pore structures for cases: (a) $\alpha = 25°$ with $b = 0.2$; (b) $\alpha = 25°$ with $b = 0.8$; and (c) $\alpha = 65°$ with $b = 0.8$.

$\alpha = 25°$ and $b = 0.8$ are narrower in the radial direction (see the pores highlighted by the black circles), resulting in the pores in the specimen with a larger b having a poorer connectivity along both the radial and vertical directions. Meanwhile, the pores in the specimen with a larger α are narrower in the circumferential direction (white circles in Figure 20b,c). The variations in the pore structures and connectivity can be explained by the same reason that accounts for the different distributions of force chains. As the radial stress σ_r increases with b, particles undergo greater compression, consequently generating more contacts and reducing the pore cavities in the radial direction. Similarly, the increased circumferential stress σ_θ and torsional stress $\tau_{z\theta}$ with α lead to a reduction in pore cavities in the circumferential direction.

It is noted that the larger the minimal distance, the larger the local pore size. When the value of distance of a voxel is larger than the sizes of fine particles, the fine particles can migrate through this voxel. In this study, a statistical index P_{vf}, that is, the percentage of voxels that allow fine particles to pass through to all voxels in layers, is defined in the following equation to better describe the connectivity of the pores along the vertical direction:

$$P_{vf} = \frac{N_{vf}}{N_v} \times 100\% \tag{24}$$

where N_{vf} is the number of voxels allowing fine particles to pass through in one layer, and N_v is the number of all voxels in this layer. When the value of P_{vf} is zero, there is no chance for fine particles to pass through this layer. Conversely, if P_{vf} is 100%, all fine particles have the potential to migrate through under the

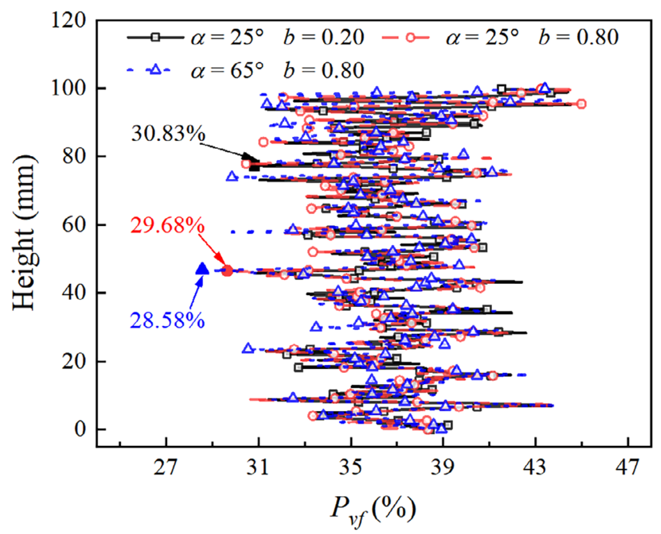

FIGURE 21 | Percent of voxels allowing fine particles to pass through in layers.

effect of seepage flow. The HCTST specimens are divided into about 650 layers along the vertical direction here. Figure 21 shows the distribution of P_{vf} in layers for the same cases as those in Figure 20. Notably, the values represented in Figure 21 are the minimal ones observed in the three cases. The values of P_{vf} are always the smallest in many layers when $\alpha = 65°$ and $b = 0.8$. This suggests an increased propensity for fine particles to be obstructed within these layers, thereby impeding their ability to migrate a long distance. In contrast, the P_{vf} values are larger in the

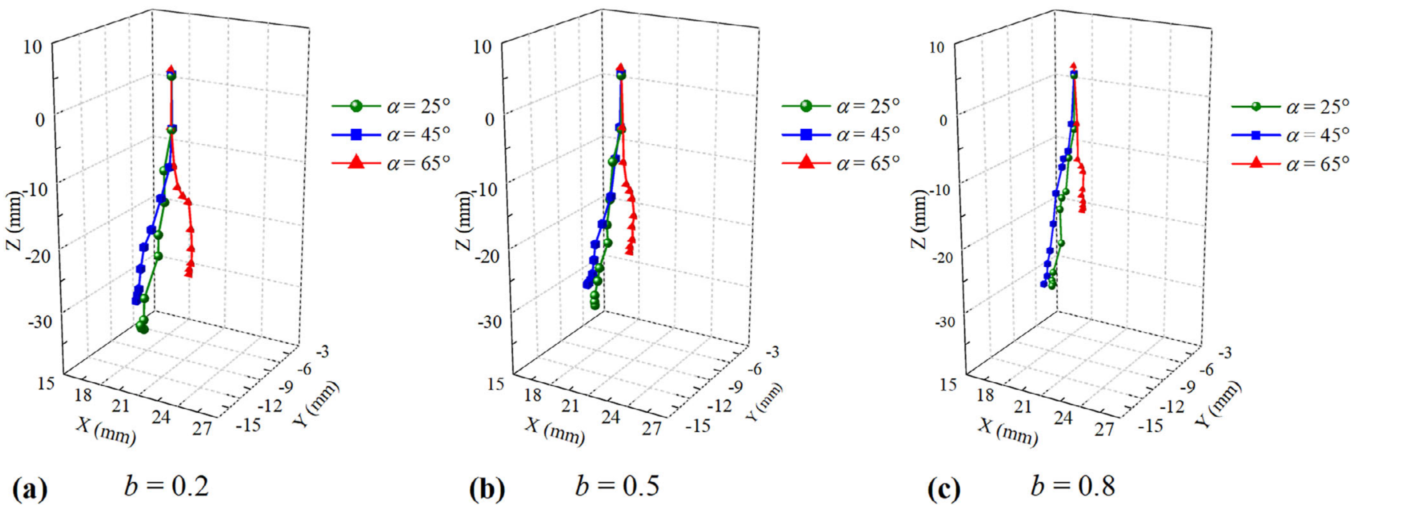

FIGURE 22 | Erosion paths of a fine particle in all cases: (a) $b = 0.2$; (b) $b = 0.5$; and (c) $b = 0.8$.

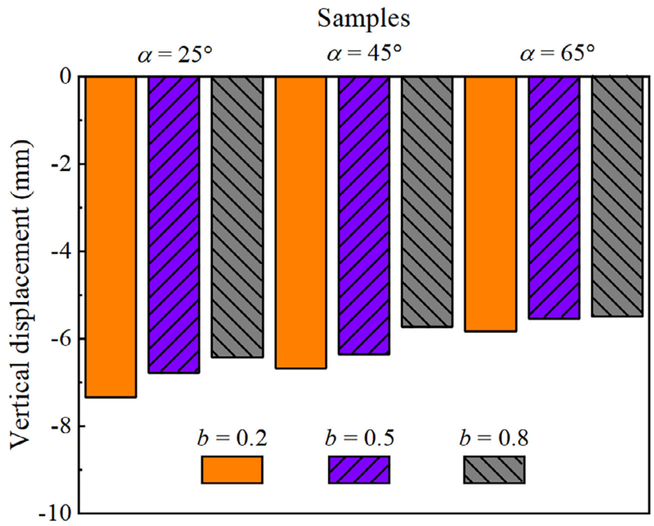

FIGURE 23 | Average vertical displacement of fine particles for all cases.

other cases, indicating enhanced connectivity along the vertical direction.

The various pore structures further cause the fine particles to migrate by the fluid along different paths, as shown in Figure 22. In this figure, the dots with different colours and shapes represent the positions of one fine particle in cases having various α and b at different suffusion moments. In general, when α and b are large, particles suffer more restriction in the horizontal plane which is perpendicular to the fluid flow, and the connectivity of pores along the vertical direction is poor. [5] Thus, the fine particles are more difficult to be washed away compared to those in the cases having smaller α and b. For example, the fine particles in the cases with $\alpha = 25°$ move a longer distance along the vertical direction, while the fine particles in the cases with larger α move a shorter distance, especially in the case with $\alpha = 65°$ and $b = 0.8$ where the fine particle is clogged after a short movement (Figure 22). Moreover, Figure 23 plots the average vertical displacement of the fine particles, showing that the fine particles in the specimens with smaller α and b travel a greater distance under the effect of seepage flow. The provided different pore structures and migration paths in the HCTST specimens under different loading conditions can to some extent explain the various fines mass loss in Figure 7.

5 | Conclusions

This study developed a stress-controlled HCTST model in DEM which can achieve the independent control of the major principal stress direction and intermediate principal stress ratio. Then, the CFD solver was introduced to conduct a series of coupled CFD-DEM simulations on gap-graded granular soils aiming to reveal the suffusion under complex loading conditions. Both macroscopic and microscopic responses during the suffusion were investigated and discussed in detail. The main findings of this study are summarized as follows:

1. Both α and b have influences on the fines mass loss. In general, fewer fine particles are washed away by the fluid as both α and b increase. The variations of the particle numbers in layers show that most eroded particles are from the layer near the CFD domain outlet, and clogging is observed in the middle layers. Meanwhile, more particles are found clogged in the middle layers as both α and b increase. In addition, the permeability of the HCTST specimens shows an increasing trend during the suffusion process, and the volume flow rates are larger in the cases having more particles loss, illustrated by the decrease of permeability with α and b.
2. Compared with coarse particles, fine particles make smaller contribution to the strong force chains, while more fine particles are observed to be strongly connected after the suffusion process. The percents of the contacts related to fine particles in strong contacts increase with α and b, implying that more fine particles are clogged and difficult to be eroded in cases having larger α and b.
3. From the microscopic perspective, the magnitudes of contact anisotropy are to some extent weakened by the fluid flow, and the corresponding principal directions slightly rotate to the

fluid direction during suffusion in all cases. In addition, more fine particles are washed away in cases whose anisotropy principal directions are close to the fluid flow direction.

4. With the increase of α, the force chains are distributed more along the horizontal direction, and the restriction on the particles from the horizontal direction increases. Meanwhile, the increased radial stress σ_r with b enhances the restriction. In addition, the pore structures also exhibit differences, and the vertical connectivity of the pores in the specimens with larger α and b is poorer.
5. The various pore structures and distributions of the contacts in specimens under different loading conditions induce fine particles to migrate along different paths, further resulting in the differences in fines mass loss and variations in particle numbers in layers.

Acknowledgements

The authors gratefully acknowledge the financial supports from the Research Grants Council of Hong Kong (Project No. 15209119, 15226322, 15229223) and the National Natural Science Foundation of China (Project No. 42207210).

Data Availability Statement

The data that support the findings of this study are available from the corresponding author upon reasonable request.

References

1. M. Foster, R. Fell, and M. Spannagle, "The Statistics of Embankment Dam Failures and Accidents," *Canadian Geotechnical Journal* 37, no. 5 (2000): 1000–1024.

2. Z. Hu, Y. Zhang, and Z. Yang, "Suffusion-Induced Evolution of Mechanical and Microstructural Properties of Gap-Graded Soils Using CFD-DEM," *Journal of Geotechnical and Geoenvironmental Engineering* 146, no. 5 (2020): 04020024.

3. Z. Huang, Y. Bai, and H. Xu, "A Vertical Layered Theoretical Model to Predict the Suffusion-Induced Heterogeneity of Cohesionless Soil," *Journal of Hydrology* 598 (2021): 126476.

4. A. Benamar and A. Bennabi, "Assessment of Suffusion Susceptibility of Soils From a British Dam," in *International Conference on Scour and Erosion* (Perth, Australia: Routledge, 2014), 189–195.

5. D. S. Chang and L. M. Zhang, "Critical Hydraulic Gradients of Internal Erosion Under Complex Stress States," *Journal of Geotechnical and Geoenvironmental Engineering* 139, no. 9 (2013): 1454–1467, https://doi.org/10.1061/(asce)gt.1943-5606.0000871.

6. Z. Hu, Y. Zhang, and Z. Yang, "Suffusion-Induced Deformation and Microstructural Change of Granular Soils: A Coupled CFD–DEM Study," *Acta Geotechnica* 14, no. 3 (2019): 795–814, https://doi.org/10.1007/s11440-019-00789-8.

7. I.-H. Kim, H.-J. Lee, and C.-K. Chung, "Assessment of the Suffusion Sensitivity of Earth-Fill Dam Soils in Korea Through Seepage Tests," in *The 29th International Ocean and Polar Engineering Conference* (Honolulu, HI: OnePetro, 2019).

8. T. Shire, C. O'Sullivan, K. Hanley, and R. Fannin, "Fabric and Effective Stress Distribution in Internally Unstable Soils," *Journal of Geotechnical and Geoenvironmental Engineering* 140, no. 12 (2014): 04014072.

9. H. Xiong, H. Wu, X. Bao, and J. Fei, "Investigating Effect of Particle Shape on Suffusion by CFD-DEM Modeling," *Construction & Building Materials* 289 (2021): 123043, https://doi.org/10.1016/j.conbuildmat.2021.123043.

10. L. Ke and A. Takahashi, "Strength Reduction of Cohesionless Soil Due to Internal Erosion Induced by One-Dimensional Upward Seepage Flow," *Soils and Foundations* 52, no. 4 (2012): 698–711.

11. J.-G. Qian, C. Zhou, Z.-Y. Yin, and W.-Y. Li, "Investigating the Effect of Particle Angularity on Suffusion of Gap-Graded Soil Using Coupled CFD-DEM," *Computers and Geotechnics* 139 (2021): 104383, https://doi.org/10.1016/j.compgeo.2021.104383.

12. J. Fonseca, C. O'Sullivan, M. R. Coop, and P. Lee, "Non-Invasive Characterization of Particle Morphology of Natural Sands," *Soils Found* 52, no. 4 (2012): 712–722.

13. R. Kuwano, L. F. Santa Spitia, M. Bedja, and M. Otsubo, "Change in Mechanical Behaviour of Gap-Graded Soil Subjected to Internal Erosion Observed in Triaxial Compression and Torsional Shear," *Geomechanics for Energy and the Environment* 27 (2021): 100197, https://doi.org/10.1016/j.gete.2020.100197.

14. D. Chang and L. Zhang, "A Stress-Controlled Erosion Apparatus for Studying Internal Erosion in Soils," *Geotechnical Testing Journal* 34, no. 6 (2011): 579–589.

15. C. Chen, L. M. Zhang, and D. S. Chang, "Stress-Strain Behavior of Granular Soils Subjected to Internal Erosion," *Journal of Geotechnical and Geoenvironmental Engineering* 142, no. 12 (2016), https://doi.org/10.1061/(asce)gt.1943-5606.0001561.

16. Y. Luo, B. Luo, and M. Xiao, "Effect of Deviator Stress on the Initiation of Suffusion," *Acta Geotechnica* 15, no. 6 (2019): 1607–1617, https://doi.org/10.1007/s11440-019-00859-x.

17. K. Cheng, Y. Wang, and Q. Yang, "A Semi-Resolved CFD-DEM Model for Seepage-Induced Fine Particle Migration in Gap-Graded Soils," *Computers and Geotechnics* 100 (2018): 30–51.

18. K. Cheng, J. Zhu, F. Qian, B. Cao, J. Lu, and Y. Han, "CFD–DEM Simulation of Particle Deposition Characteristics of Pleated Air Filter Media Based on Porous Media Model," *Particuology* 72 (2023): 37–48.

19. N. Abdoulaye Hama, T. Ouahbi, S. Taibi, H. Souli, J.-M. Fleureau, and A. Pantet, "Analysis of Mechanical Behaviour and Internal Stability of Granular Materials Using Discrete Element Method," *International Journal for Numerical and Analytical Methods in Geomechanics* 40, no. 12 (2016): 1712–1729.

20. F. Chen, "Coupled Flow Discrete Element Method Application in Granular Porous media Using Open Source Codes," (Phd diss., University of Tennessee, 2009): 21.

21. Z. Ma, Y. Wang, N. Ren, and W. Shi, "A Coupled CFD-DEM Simulation of Upward Seepage Flow in Coarse Sands," *Marine Georesources & Geotechnology* 37, no. 5 (2019): 589–598.

22. H. Xiong, Z. Zhang, X. Sun, Z.-Y. Yin, and X. Chen, "Clogging Effect of Fines in Seepage Erosion by Using CFD–DEM," *Computers and Geotechnics* 152 (2022): 105013.

23. H. Xiong, Z.-Y. Yin, J. Zhao, and Y. Yang, "Investigating the Effect of Flow Direction on Suffusion and Its Impacts on Gap-Graded Granular Soils," *Acta Geotechnica* 16, no. 2 (2020): 399–419, https://doi.org/10.1007/s11440-020-01012-9.

24. P. Wang, Y. Ge, T. Wang, Q.-W. Liu, and S.-X. Song, "CFD-DEM Modelling of Suffusion in Multi-Layer Soils With Different Fines Contents and Impermeable Zones," *Ournal of Zhejiang University-Science A* 24, no. 1 (2023): 6–19.

25. J. Zhao and T. Shan, "Coupled CFD–DEM Simulation of Fluid–Particle Interaction in Geomechanics," *Powder Technology* 239 (2013): 248–258.

26. Z. Hu, J. Z. Li, Y. D. Zhang, Z. X. Yang, and J. K. Liu, "A CFD–DEM Study on the Suffusion and Shear Behaviors of Gap-Graded Soils Under Stress Anisotropy," *Acta Geotechnica* 18 (2022): 3091–3110, https://doi.org/10.1007/s11440-022-01755-7.

27. Y. Liu, L. Wang, Y. Hong, J. Zhao, and Z. Y. Yin, "A Coupled CFD-DEM Investigation of Suffusion of Gap Graded Soil: Coupling Effect of Confining Pressure and Fines Content," *International Journal for Numerical and Analytical Methods in Geomechanics* 44, no. 18 (2020): 2473–2500, https://doi.org/10.1002/nag.3151.

28. C. Zhou, J. G. Qian, and Z. Y. Yin, "Microscopic Investigation of the Influence of Complex Stress States on Internal Erosion and Its Impacts on Critical Hydraulic Gradients," *International Journal for Numerical and Analytical Methods in Geomechanics* 46, no. 18 (2022): 3377–3401, https://doi.org/10.1002/nag.3454.

29. Y. Liu, Z.-Y. Yin, L. Wang, and Y. Hong, "A Coupled CFD–DEM Investigation of Internal Erosion Considering Suspension Flow," *Canadian Geotechnical Journal* 58, no. 9 (2021): 1411–1425.

30. H. Zhou, G. Wang, C. Jia, and C. Li, "A Novel, Coupled CFD-DEM Model for the Flow Characteristics of Particles Inside a Pipe," *Water* 11, no. 11 (2019): 2381, https://doi.org/10.3390/w11112381.

31. Y. Peng, X. Ding, Z.-Y. Yin, and P. Wang, "Micromechanical Analysis of the Particle Corner Breakage Effect on Pile Penetration Resistance and Formation of Breakage Zones in Coral Sand," *Ocean Engineering* 259 (2022): 111859.

32. P. Wang, Z.-Y. Yin, and Z.-Y. Wang, "Micromechanical Investigation of Particle-Size Effect of Granular Materials in Biaxial Test With the Role of Particle Breakage," *Journal of Engineering Mechanics* 148, no. 1 (2022), https://doi.org/10.1061/(asce)em.1943-7889.0002039.

33. H. Jasak, A. Jemcov, and Z. Tukovic, "OpenFOAM: A C++ Library for Complex Physics Simulations," in *International Workshop on Coupled Methods in Numerical Dynamics* (Dubrovnik, Croatia: University of Zagreb, Faculty of Mechanical Engineering and Naval Architecture, 2007), 1–20.

34. R. Di Felice, "The Voidage Function for Fluid-Particle Interaction Systems," *International Journal of Multiphase Flow* 20, no. 1 (1994): 153–159.

35. S. Ergun, "Fluid Flow Through Packed Columns," *Chemical Engineering Progress* 48, no. 2 (1952): 89.

36. A. M. Brosse, *Study of the Anisotropy of Three British Mudrocks Using a Hollow Cylinder Apparatus* (London: Imperial College London, 2012).

37. S. Song, P. Wang, Z. Yin, and Y. P. Cheng, "Micromechanical Modeling of Hollow Cylinder Torsional Shear Test on Sand Using Discrete Element Method," *Journal of Rock Mechanics and Geotechnical Engineering* Published ahead of print, April 23, 2024, https://doi.org/10.1016/j.jrmge.2024.02.010.

38. D. Hight, A. Gens, and M. Symes, "The Development of a New Hollow Cylinder Apparatus for Investigating the Effects of Principal Stress Rotation in Soils," *Geotechnique* 33, no. 4 (1983): 355–383.

39. L. Yang, *Experimental Study of Soil Anisotropy Using Hollow Cylinder Testing* (Nottingham: University of Nottingham, 2013).

40. B. Li, L. Guo, and F.-s. Zhang, "Macro-Micro Investigation of Granular Materials in Torsional Shear Test," *Journal of Central South University* 21, no. 7 (2014): 2950–2961, https://doi.org/10.1007/s11771-014-2262-3.

41. J. Zhang, X. Wang, Z.-Y. Yin, and Z. Liang, "DEM Modeling of Large-Scale Triaxial Test of Rock Clasts Considering Realistic Particle Shapes and Flexible Membrane Boundary," *Engineering Geology* 279 (2020): 105871.

42. J. P. de Bono and G. R. McDowell, "DEM of Triaxial Tests on Crushable Sand," *Granular Matter* 16, no. 4 (2014): 551–562, https://doi.org/10.1007/s10035-014-0500-x.

43. P. Wang, C. Xu, Z.-Y. Yin, S.-X. Song, C. Xu, and S. Dai, "A DEM-Based Generic Modeling Framework for Hydrate-Bearing Sediments," *Computers and Geotechnics* 171 (2024): 106287, https://doi.org/10.1016/j.compgeo.2024.106287.

44. K. Miura, S. Miura, and S. Toki, "Deformation Behavior of Anisotropic Dense Sand Under Principal Stress Axes Rotation," *Soils and Foundations* 26, no. 1 (1986): 36–52, https://doi.org/10.3208/sandf1972.26.36.

45. J. Zhang, X. Wang, Z.-Y. Yin, and Z. Liang, "DEM Modeling of Large-Scale Triaxial Test of Rock Clasts Considering Realistic Particle Shapes and Flexible Membrane Boundary," *Engineering Geology* 279 (2020): 105871, https://doi.org/10.1016/j.enggeo.2020.105871.

46. R. Fannin and R. Moffat, "Observations on Internal Stability of Cohesionless Soils," *Geotechnique* 56, no. 7 (2006): 497–500.

47. T. Kenney and D. Lau, "Internal Stability of Granular Filters: Reply," *Canadian Geotechnical Journal* 23, no. 3 (1986): 420–423.

48. Y. Liu, Z.-Y. Yin, and J. Yang, "Micromechanical Analysis of Suffusion in Gap-Graded Granular Soils Considering Soil Heterogeneity and non-Uniform Seepage Flow," *Computers and Geotechnics* 159 (2023): 105467.

49. P. A. Cundall and O. D. Strack, "A Discrete Numerical Model for Granular Assemblies," *Geotechnique* 29, no. 1 (1979): 47–65.

50. Y. Liu, L. Wang, Z.-Y. Yin, and Y. Hong, "A Coupled CFD-DEM Investigation Into Suffusion of Gap-Graded Soil Considering Anisotropic Stress Conditions and Flow Directions," *Acta Geotechnica* 18 (2022): 3111–3132, https://doi.org/10.1007/s11440-022-01734-y.

51. T. Wang, P. Wang, Y. Z-y, F. Laouafa, and P.-Y. Hicher, "Hydro-Mechanical Analysis of Particle Migration in Fractures With CFD-DEM," *Engineering Geology* 335 (2024): 107557.

52. F. Radjai, D. E. Wolf, M. Jean, and J.-J. Moreau, "Bimodal Character of Stress Transmission in Granular Packings," *Physical Review Letter* 80, no. 1 (1998): 61.

53. N. H. Minh, Y. P. Cheng, and C. Thornton, "Strong Force Networks in Granular Mixtures," *Granular Matter* 16, no. 1 (2013): 69–78, https://doi.org/10.1007/s10035-013-0455-3.

54. A. Tordesillas, "Force Chain Buckling, Unjamming Transitions and Shear Banding in Dense Granular Assemblies," *Philosophical Magazine* 87, no. 32 (2007): 4987–5016.

55. H. Dong and M. J. Blunt, "Pore-Network Extraction From Micro-Computerized-Tomography Images," *Physical Review E—Statistical, Nonlinear, and Soft Matter Physics* 80, no. 3 (2009): 036307.

56. D. B. Silin, G. Jin, and T. W Patzek, "Robust Determination of the Pore Space Morphology in Sedimentary Rocks," in *SPE Annual Technical Conference and Exhibition, Proceedings-Mile High Meeting of the Minds* (Denver, CO: SPE, 2003), SPE-84296-MS.

57. D. Silin and T. Patzek, "Pore Space Morphology Analysis Using Maximal Inscribed Spheres," *Physica A: Statistical Mechanics and Its Applications* 371, no. 2 (2006): 336–360, https://doi.org/10.1016/j.physa.2006.04.048.

58. F. Arand and J. Hesser, "Accurate and Efficient Maximal Ball Algorithm for Pore Network Extraction," *Computers & Geosciences* 101 (2017): 28–37.